03,13,14

Band Structure and Mechanical Properties of Orthorhombic $LiAlS_2$ Crystal

© E.B. Duginova[1], Yu.M. Basalaev[1,2], N.G. Kravchenko[3], E.V. Duginov[1]

[1] T.F. Gorbachev Kuzbass State Technical University,
Kemerovo, Russia
[2] Russian State Agrarian University — Moscow Timiryazev Agricultural Academy,
Moscow, Russia
[3] Kemerovo State University,
Kemerovo, Russia

E-mail: kit.katy@mail.ru

Received January 2, 2025
Revised January 2, 2026
Accepted February 1, 2026

For the first time, the equilibrium lattice parameters for the orthorhombic $LiAlS_2$ crystal have been obtained using density functional theory methods. The energy band structure of the crystal and its sublattices have been calculated, and plots of the density of states and maps of the deformation charge density of valence electrons have been constructed. Using the PBE functional and a full-valence basis set, the band gap width $E_g = 4.58$ eV has been calculated. The elastic properties of the crystal have been studied, and the values of the optical lattice vibration frequencies have been found. A comparison of the band spectra of the tetragonal and orthorhombic $LiAlS_2$ crystals has been carried out.

Keywords: lithium aluminum disulfide, $LiAlS_2$, band structure.

DOI: 10.61011/PSS.2026.02.63379.8999

1. Introduction

Lithium and aluminum disulfide ($LiAlS_2$) was initially considered as a promising material for fabrication of solid electrolytes [1]. The experimental study in [1] of the aluminum sulfide ternary systems M_2S-Al_2S_3, where $M =$ Li, Na, K ($LiAlS_2$, $NaAlS_2$, $KAlS_2$) demonstrated the existence of not only electronic conductivity phases, but also phases with an ionic conductivity. Technological growth has dictated the need for developing new nonlinear optical (NLO) materials, among which special attention is paid to the nonlinear crystals, in particular $LiMX_2$ (where $M =$ Al, In, Ga; $X =$ s, Se, Te), which is critical in fabrication of new light sources [2–5] capable of emitting in the ranges of deep ultraviolet DUV (Deep ultraviolet, $100-300$ nm), as well as medium($1.4-3\,\mu$m) and far ($3-50\,\mu$m) infrared (IR) ranges [6,7]. Due to these properties, IR NLO materials have found wide application in a number of civil and defense fields, including laser guidance, environmental monitoring, and laser medicine [8–11].

Ternary chalcogenides with its chemical formula AMX_2, where A includes the elements of the I group of periodic table (Li, Ag, Cu and etc.), M represents the metal of the III group (Al, In, Ga), and X includes chalcogenides (S, Se, Te), belong to the diamond-like compounds family I-III-VI_2 and today are well known and studied. Among them, crystals with chalcopyrite structure are the most demanded, due to their wide application in photovoltaics and thermoelectrics [12–16]. The advantage of using AMX_2 crystals, for example, in solar cell devices, is their high stability, environmental safety, prevalence and availability of the chemical elements included in their composition. $AgGaS_2$ is considered the most in-demand among IR NLO crystals, with high NLO characteristics, but with a significant disadvantage — low threshold of laser damage, which is, in particular, explained by the small band gap of a crystal, and prevents its use in high-energy laser systems.

For photovoltaic applications, it is important to obtain a working material with the required spectral range. Since AMX_2 crystals are synthesized in various chemical compositions, their band gap can be adjusted to a certain spectral range by replacing X anions and A and M metals.

Ternary compounds $LiMX_2$ are isoelectronic analogues of diamond-like compounds $AgMX_2$ and $CuMX_2$, however, they exhibit a wider band gap and, consequently, a higher threshold for laser-induced damage compared to series containing Ag and Cu. It has been experimentally established that, as a rule, $LiMX_2$ compounds, as well as their analogues $AgMX_2$ and $CuMX_2$, crystallize into cubic, tetragonal, hexagonal, rhombic and rhombohedral structures. So far, not all physical and chemical properties of $LiMX_2$ compounds ($M =$ B, Al, Ga, In; $X =$ O, S, Se, Te) with an orthorhombic structure have been systematically studied [2–5,17,18], namely, this is the case of $LiAlS_2$ crystal, with no any experimental data on its characteristics, including the band gap width, available in the literature [19–21]. The presence of the lightest metals (Li and Al) in $LiAlS_2$ crystal provides a shorter cutoff boundary in the visible or ultraviolet region of the spectrum. The large band gap, absence of two-photon absorption, and

high threshold of laser-induced damage established for non-orthorhombic structures make $LiAlS_2$ a promising material for the high-energy laser systems.

Another essential application of $LiAlS_2$ crystal and its analogues is the use as renewable and environmentally friendly alternative energy sources. Triple chalcogenides $LiMX_2$ are considered as one of the promising working materials for third-generation solar cells. The rhombohedral structure of chalcogenides $LiMX_2$ has been investigated in the experimental and theoretical studies in the last decade [20–26]. The research has shown that the ternary chalcogenides in this structure exhibit interesting photoelectric properties. The synthesis of orthorhombic phase of $LiAlS_2$ was first mentioned as early as in 1979 [1]. New phases of $LiAlS_2$ have been identified, as well as the lattice parameters and the density of the synthesized compound has been found.

In paper [27] published in 2005, it was pointed out that the synthesis of the orthorhombic structure in the laboratory had not yet been possible due to the instability of $LiAlS_2$, which the authors explained by the discrepancy between the sizes of aluminum ions and the size of tetrahedral gaps in the lattice.

In the theoretical study [16], ternary sulfides with diamond-like structures suitable for use in nonlinear optics in the spectral region of the mid-infrared range were studied. The authors concluded that the determining factor of nonlinear optical effects in diamond-like metal sulfides is not the location itself, but rather the type of tetrahedra $[MS_4]$, almost irrespective of the structural symmetry details. It is emphasized that silver-containing compounds have a smaller band gap compared to lithium-containing compounds, but at the same time, data on the lattice parameters of orthorhombic chalcogenide $LiAlS_2$ are not outlined in [16].

The monoclinic structure of Li_5AlS_4 sulfide was studied in [28], where it was compared with the structures of various lithium-containing sulfides, also with a group of crystals $LiMS_2$ ($M = $ Al, Ga, In). This comparison allowed the authors to establish a correlation between ion transport and distribution of lithium atoms in sulfides of various structures.

In [29] outlines a comprehensive study of thermodynamics and kinetics at the cathode-electrolyte interface in the solid-state lithium-sulfur batteries, performed using a density functional theory analysis. The results obtained by the authors showed that among the main types of solid electrolytes (oxides, sulfides, nitrides, halides), it is sulfide solid electrolytes that demonstrate the greatest stability. The authors [29] concluded that $LiAlS_2$ crystal, similar to the other ternary or binary sulfides may serve an excellent buffer layer.

The synthesis of the orthorhombic phase $LiAlS_2$ was performed in 2023 [30] using a two-zone Bridgman-Stockbarger furnace, where crystals of several millimeters in size were obtained. In addition to synthesis, the authors made *ab initio* calculations for an experimentally found crystal structure using CASTEP package. In this calculations they used GGA approximation and exchange-correlation functional Perdew-Burke-Ernzerhof (PBE). The paper describes the parameters of the lattice, band gap, and the optical properties of $LiAlS_2$. The authors of [30], as well as the authors of [16], note that $LiAlS_2$ has the widest band gap of 5.13 eV among the selected IR NLO materials and an exceptionally high threshold of laser damage, approximately 28 times higher than $AgGaS_2$, and also that it is the tetrahedra of $[AlS_4]$ that determine the band gap width.

A general analysis of the publications showed that none of the papers provided the atomic coordinates, no lengths of Li-S and Al-S bonds were specified, and no any studies of the vibrational and elastic properties of the orthorhombic crystal $LiAlS_2$ were performed. The purpose of our work is a theoretical study of the band structure, calculation and analysis of vibrational, as well as elastic characteristics for the orthorhombic phase of $LiAlS_2$ using CRYSTAL [31] and Quantum Espresso software packages [32].

2. Model and calculation parameters

The electronic structure and frequency characteristics for $LiAlS_2$ crystal were calculated using CRYSTAL [31] and Quantum Espresso [32] software. Both software codes use density functional theory (DFT) methods. The calculations used different functionals and approximations implemented in CRYSTAL and Quantum Espresso codes: LDA (local density approximation), GGA (generalized gradient approximation), PBE (Perdew-Burke-Ernzerhof). In Quantum Espresso the PBE functionals and LDA approximation were used with different potentials: for LDA — Perdew-Zunger (pz); and for PBE — ultra-soft Kresse and Joubert potential PAW (kjpaw), as well as nonrelativistic norm-preserving Martins-Troullier (mt) pseudopotentials.

The Brillouin zone partition is made on a grid of special points $16 \times 16 \times 16$. Overall, convergence in total energy was not worse than 10^{-3} eV/atom, and in phonon frequencies within tenths of cm^{-1}. All calculations in CRYSTAL code were made using a full-electron split-valence basis of Gaussian orbitals TZVP (Triple-Zeta Valence with Polarization).

The electronic configuration of atoms is defined as follows: Li $(1s^2 2s^2 2p^1)$, Al $(1s^2 2s^2 2p^6 3s^2 3p^1)$, S $(1s^2 2s^2 2p^6 3s^2 3p^4)$. The Brillouin zone for the structure of sodium β-ferrite (β-$NaFeO_2$) with a dedicated irreducible part and basic high degree symmetry points:

$\Gamma = (0\,0\,0)$; $Z = (0\ 0\ 1/2)$; $X = (1/2\ 0\ 0)$; $Y = (0\ 1/2\ 0)$; $S = (1/2\ 1/2\ 0)$; $T = (0\ 1/2\ 1/2)$; $U = (1/2\ 0\ 1/2)$; $R = (1/2\ 1/2\ 1/2)$, in units $(2\pi/a; 2\pi/b; 2\pi/c)$, is shown in Figure 1.

3. Crystal structure

Structure of $LiAlS_2$ crystal in βphase of $NaFeO_2$ is the orthorhombic itself with a spatiotemporal group C_{2v}^9 (or $Pna2_1$, No. 33). The lattice is shown in Figure 2. The unit cell of crystals β-$NaFeO_2$ contains 16 atoms (32 valence electrons). Coordination number is equal 4, and coordination polyhedron — tetrahedron (Figure 2). The number of formula units in the film is 4.

Table 1. Crystal structure parameters of $LiAlS_2$

$LiMX_2$	LDA (QE)	LDA	PBE (QE)		PBE	Experiment	
	pz	(CR)	mt	kjpaw	(CR)	[24]	[30]
a, (Å)	6.5214	6.4775	6.6628	6.6766	6.5887	6.484	6.4841(3)
b, (Å)	8.1786	7.9142	8.2765	8.2438	8.0465	7.875	7.8635(3)
c, (Å)	4.9707	6.1706	5.8020	5.6868	6.2730	6.188	6.1797(3)
c/a	0.7622	0.9526	0.8708	0.8517	0.9521	0.9543*	0.9531*
b/a	1.2541	1.2218	1.2422	1.2347	1.2213	1.2145*	1.2127*
δ	0.0687	0.0476	0.0610	0.0561	0.0472	0.0427*	0.0414*

The lattice of type β-$NaFeO_2$ has the basic structure of wurtzite, but with the ordering of cations at tetrahedral positions and natural deformation along b axis, determined by the interatomic interaction in the second coordination sphere. Such a natural deformation leads to a decline in symmetry and it becomes an orthorhombic one, and the concept of „orthorhombic extension“ $\delta = \frac{\sqrt{3}}{2} - \frac{a}{b}$ is introduced to characterize it. This ordering of cations leads to a decrease in symmetry to orthorhombic. The unit cell contains: two layers of closely-packed atoms of anions on heights 0 and 1/2 (in units c); two layers of cations on heights 1/6 and 2/3 (ideally, without taking into account the differences in the size of the cations). Cations located, for example, at a height of 1/6 are coordinated with three anion atoms at a height of 0 and one anion atom at a height of 1/2, while each tetrahedron contains two unequal anion atoms, all tetrahedra of AlS_4 are directed upward, along z axis, and are connected to each other through common vertices.

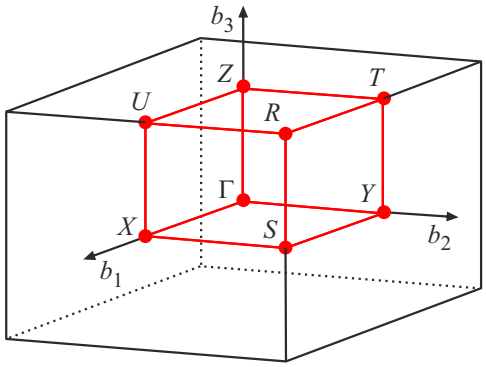

Figure 1. Brillouin zone of sodium β-ferrite (β-$NaFeO_2$) [33].

Positions of the atoms of the orthorhombic phase of $LiAlS_2$, in units (a, b, c), can be set as follows:

Li: $(x, y, z)(-x, -y, z+1/2)(x+1/2, -y+1/2, z)(-x+1/2, y+1/2, z+1/2)$,

Al: $(x, y, z)(-x, -y, z+1/2)(x+1/2, -y+1/2, z)(-x+1/2, y+1/2, z+1/2)$,

S1: $(x, y, z)(-x, -y, z+1/2)(x+1/2, -y+1/2, z)(-x+1/2, y+1/2, z+1/2)$,

S2: $(x, y, z)(-x, -y, z+1/2)(x+1/2, -y+1/2, z)(-x+1/2, y+1/2, z+1/2)$,

where $(x,\ y,\ z)$ — coordinates of atoms in the lattice.

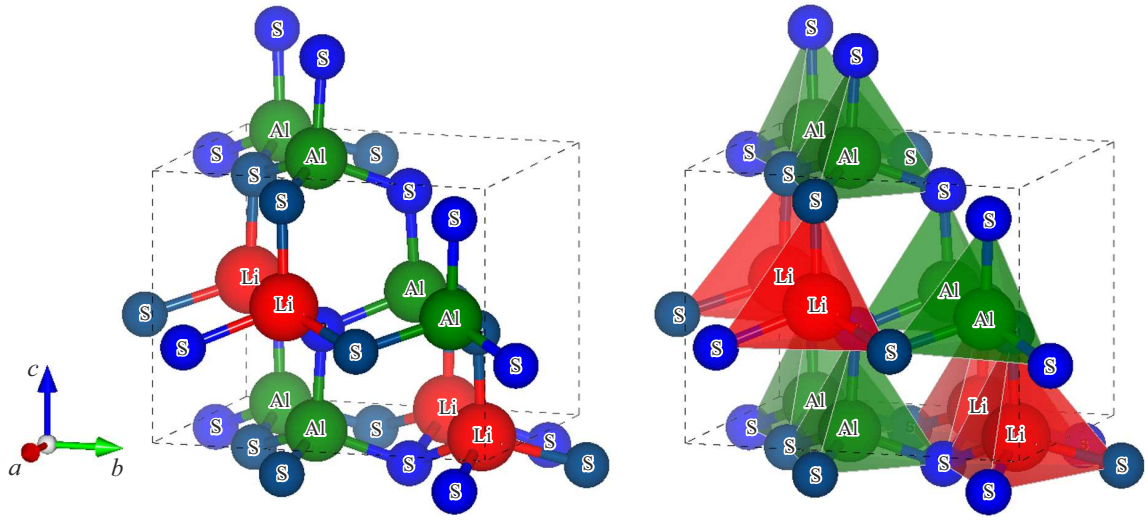

Figure 2. Lattice and cation tetrahedrons of the orthorhombic crystal of $LiAlS_2$ (plotted using VESTA [34]).

Table 2. Calculated atomic coordinates and bond lengths of an orthorhombic crystal

Atoms	x	y	z	Al-S, Å		Li-S, Å	
Li	0.0853	0.6204	0.6151	(1)	2.2822	(1)	2.4638
Al	0.0722	0.1259	0.6216	(1')	2.2976	(1')	2.4773
S1	0.0611	0.1140	0.9874	(2)	2.2923	(2)	2.4895
S2	0.0961	0.6402	0.0109	(2')	2.2962	(2')	2.5001

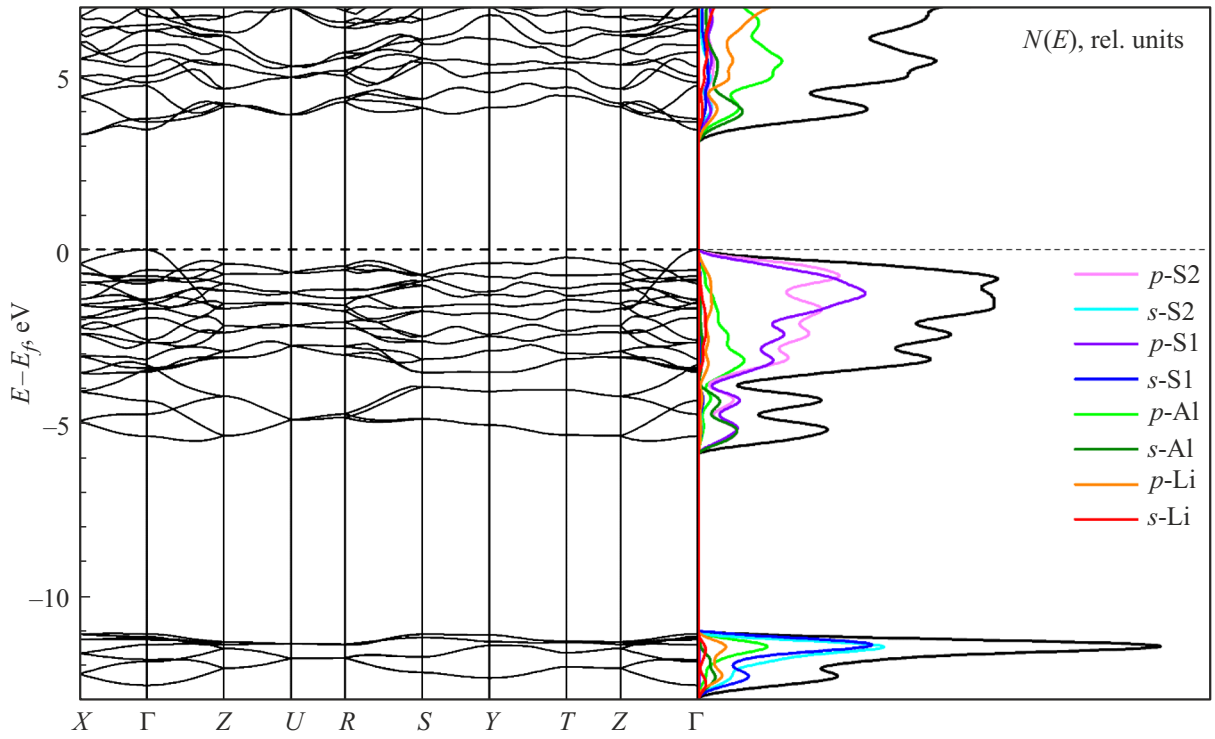

Figure 3. The band structure and the density of states of $LiAlS_2$ crystal analyzed using Quantum Espresso program code (pseudopotential — mt).

The lattice parameters calculated using standard CRYSTAL (CR) and Quantum Espresso (QE) codes improvement procedures and experimental data from [24] and [30] are shown in Table 1.

As can be seen from Table 1, all the calculated values of a, b, c are generally comparable with experimental data. At that, the missing values calculated according to experimental data are marked with an asterisk.

Table 2 shows the coordinates of atoms that form $LiAlS_2$ crystal. The structure of $LiAlS_2$ compound is a 3D carcass made of distorted tetrahedra LiS_4 and AlS_4, connected with each other via common vertices (Figure 2). The distances Li-S here lie in the range 2.4638−2.5001Å, whereas distances Al-S make from 2.2822 to 2.2976 Å for the tetrahedra LiS_4 and AlS_4 respectively (Figure 2). Due to the fact that tetrahedra consist of four anions (two nonequivalent ones), the bond lengths are also four, while equivalent atoms are indicated by the symbol «'» (Table 2). The structure of $LiAlS_2$ is characterized by a dense hexagonal packing of anions, which should ensure good chemical stability of the compound.

4. Band structure

The energy band structure of the orthorhombic crystal $LiAlS_2$ and its sublattices were calculated at the points of high symmetry of the irreducible part of the Brillouin zone (highlighted part, Figure 1) and along the lines connecting them. The calculated band structure, together with the total and partial densities of states $N(E)$ of $LiAlS_2$crystal, calculated using the Quantum Espresso program code, are shown in Figure 3. The beginning of the energy scale is aligned with the last filled state. The density of $N(E)$ is normalized to the full number of states included in the calculation.

Table 3. The following band gap values were obtained E_g (eV) for $LiAlS_2$

LDA		PBE		
QE (pz)	CR (TZVP)	QE (mt)	QE (kjpaw)	CR (TZVP)
2.65 (Γ-Γ)	4.39	3.46 (Γ-Γ)	3.54 (Γ-Γ)	4.58
2.10 (Γ-X)	–	3.32 (Γ-X)	3.23 (Γ-X)	–
Experiment 5.13 eV [30]		Theory CASTEP (PBE) 4.13 eV [30]		

The valence band of the orthorhombic crystal $LiAlS_2$ contains 32 valence electrons, which are distributed over the corresponding 16 energy levels (Figure 3), divided into three main subbands. The lower subband of eight energy levels, in the range from −13 to −11 eV, originates from 3*s*-states of S atoms that define the bottom of the valence band of $LiAlS_2$ crystal. The forbidden energy interval between the lower subband and the rest of the valence band is 5.7 eV. The subband lying in the region from −3.5 to −6 eV, has a characteristic shape and contains four energy levels which originate from 3*s*-states of Al atoms. This subband overlaps with the upper valence subband of twenty levels, which is formed by 3*p* states of S atoms and, to a lesser extent, Al atoms. The upper levels of the valence band are completely formed by 3*p*-states of sulfur, the top of the valence band is located at the point Γ.

The analysis of the total density of states $N(E)$, taking into account the partial contributions of atoms forming the orthorhombic crystal $LiAlS_2$, allowed us to supplement the data on its band structure and clarify the contributions of individual atoms to the valence band and conduction band. The main conclusions were generally proved, and it was found that the contributions of 3*s* states of the unequal S1 and S2 atoms were concentrated in the region of the lower subband of the valence band and actually coincided. The contributions of 3*p*-states of S atoms form mainly the tip of the valence band and differ significantly. For 3*s*- and 3*p*-states of Al atoms, the distribution of contributions in the upper and middle subband is observed. The bottom of the conduction band contains mainly contributions of *p*-states of both cations (Li and Al). The sublattice of Li atoms has little effect on the formation of the structure of the crystal's energy spectrum.

The conduction band has an absolute minimum at *X*, which is separated from the tip of the valence band at point Γ by a value of 3.23 eV (Γ-*X*), which is slightly less than the direct transition at point Γ — 3.54 eV (Γ-Γ), therefore, the orthorhombic crystal $LiAlS_2$ is itself an indirect band gap wide-band semiconductor.

The values of the band gap (E_g) of $LiAlS_2$ crystal found using various functionals and approximations in CRYSTAL (CR) and Quantum Espresso (QE) program codes are illustrated in Table 3. The worst scenario was from Quantum Espresso in LDA — Perdew-Zunger (pz) approximation, where E_g was two times less than the experimental value [30]. The use of non-relativistic norm-preserving Martins-Trullier pseudopotentials (mt) and ultra-soft Kress and Joubert potentials PAW (kjpaw) in combination with PBE functional brings the calculated values E_g closer to the experimental value. The best results E_g were obtained in CRYSTAL code were made using a full-electron split-valence basis of Gaussian orbitals TZVP (Triple-Zeta Valence with Polarization).

The orthorhombic structure of β-$NaFeO_2$ of $LiAlS_2$ crystal differs from the tetragonal structure similar to chalcopyrite in that the S anions, equivalent in the chalcopyrite structure, become unequal in the orthorhombic structure and are divided into two unequal sublattices S1 and S2. Such a structural difference is manifested in the bands structure as the „doubling effect". Since β-$NaFeO_2$ type structure can be considered a derivative of the tetragonal one, it is of interest to consider the $LiAlS_2$ crystal bands in both phases. For tetragonal structures, the most important direction is along the crystal main axis (z axis) and perpendicular to it, therefore, with respect to the bands structure, two mutually perpendicular directions will be the most informative: along $\Gamma \to Z$ and $\Gamma \to X$ lines.

The calculated band structure $E(\mathbf{k})$ of tetragonal (D_{2d}^{12}) [35] and orthorhombic (C_{2v}^{9}) $LiAlS_2$ crystal with the main sublattices are shown in Figure 4. The sublattices method was developed mainly for analyzing the charge distribution of valence electrons and allowing for the role of unequal sublattices in the formation of chemical bonds in crystals of various compositions [36–40]. In this case, we used a technique from [40] where the band structure of ABX_2 crystal is obtained from the band structure of sublattices of individual atoms(A, B, X) and sublattice systems such as cationic tetrahedra (AX_4 and BX_4). This approach makes it possible to trace the participation of atomic sublattices in formation of the crystal band spectrum and, in particular, in formation of the valence band.

Calculations have shown that the valence band of $_2$ crystal in tetragonal (D_{2d}^{12}) [35] and orthorhombic (C_{2v}^{9}) phases has the same energy range — about 13 eV, which is determined by the position of 3*s*-state (lower bound) and 3*p*-state (upper bound) of S anion. A comparison of the valence bands of both phases (Figure 4) proves the similarity of crystal structures, as well as the difference in the number of valence electrons (16 and 32), which naturally leads to the „doubling effect" observed in the orthorhombic phase (C_{2v}^{9}).

The characteristic 3*s*-band of the corresponding states of Al atoms in the tetrahedra of AlS_4 retains its structure, approaches 3*p*-states of S atoms and does not change its identity, as well as its energy arrangement, after formation of tetrahedra of LiS_4 crystal. The effect of the sublattice of Li atoms is not significant, and the valence band formed during formation of AlS_4 tetrahedra does not change at all, Li^+ cations fill the voids between tetrahedra of AlS_4 and generally ensure the electroneutrality of $LiAlS_2$ crystal.

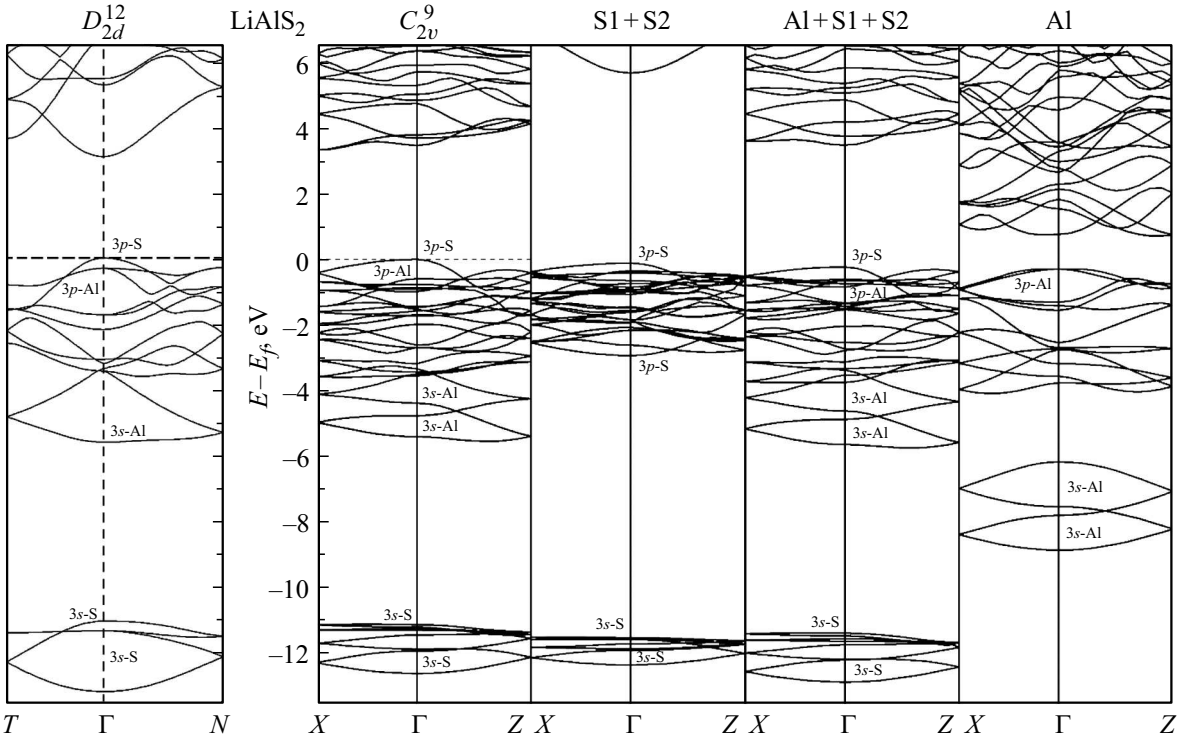

Figure 4. Band structure of tetragonal (D_{2d}^{12}) [35] and orthorhombic (C_{2v}^{9}) crystal $LiAlS_2$, atomic sublattices (Al and S1 + S2) and cation tetrahedra AlS_4 (Al + S1 + S2) calculated using Quantum Espresso code (pseudopotential — mt).

5. Chemical bond

To obtain electron density distribution charts and chemical bond analysis in $LiAlS_2$ crystal, two approaches were used based on calculating the deformation [31] and difference [41] density of charge distribution of valence electrons $\Delta\rho^{\text{def}}(\mathbf{r})$ and $\Delta\rho(\mathbf{r})$. The difference between these densities is that the deformation electron density characterizes the redistribution of the electron density in a real crystal relative to the model of free atoms [31]:

$$\Delta\rho^{\text{def}}(\mathbf{r}) = \rho^{\text{LiAlS2}}(\mathbf{r}) - \rho_{\text{Li}}(\mathbf{r}) - \rho_{\text{Al}}(\mathbf{r}) - \rho_{\text{S}}(\mathbf{r}).$$

The difference electron density takes into account the hybridization effects in the sublattices and is calculated as the difference between the electron density of the crystal and its sublattices:

$$\Delta\rho(\mathbf{r}) = \rho^{\text{cryst}}(\mathbf{r}) - \Sigma\rho_n^{\text{sub}}(\mathbf{r}).$$

In general, the deformation and difference electron densities give qualitatively similar patterns of electron density redistribution during crystal formation and demonstrate the charge distribution of valence electrons, taking into account the effects of chemical bonding.

The deformation $\Delta\rho^{\text{def}}(\mathbf{r})$(2D) electron density calculated using CRYSTAL (CR) code [31] and difference $\Delta\rho(\mathbf{r})$(3D) electron density found using Quantum Espresso (QE) [32] for $LiAlS_2$ crystal are illustrated in Figure 5. The deformation electron density isolines are drawn in increments of 0.01 a.u., the dashed line corresponds to $\Delta\rho^{\text{def}}(\mathbf{r}) = 0$, the dotted line — $\Delta\rho^{\text{def}}(\mathbf{r}) < 0$, while solid line stands for $\Delta\rho^{\text{def}}(\mathbf{r}) > 0$.

Each atom in the orthorhombic $LiAlS_2$ crystal, as well as in the tetragonal $LiAlS_2$ crystal with the chalcopyrite structure [35], is surrounded by four atoms of a different grade, i. e., it has a diamond-like structure which is illustrated in $\Delta\rho^{\text{def}}(\mathbf{r})$ charts of the orthorhombic phase in the form of zigzag chains typical of all diamond-like compounds along cation-anion bonds -Li-S-Al-S-Li-. The bonds between the closest neighbors in tetrahedra of LiS_4 and AlS_4 because of the non-equivalency of sulfur sub-lattices (S1 and S2) have different lengthsLi-S and Al-S (Table 2). Localized maxima of covalent charge density are located on the bond lines Li-S and Al-S, shifted relative to the bond center towards the anion (S). The shift value correlates with the degree of ionic bonding, estimated by Polling formulas [42]

$$I_{\text{LiS}} = 1 - \exp(-\alpha(\chi_{\text{Li}} - \chi_{\text{S}})^2) = 0.48$$

$$\text{and } I_{\text{AlS}} = 1 - \exp\left(-\alpha(\chi_{\text{Al}} - \chi_{\text{S}})^2\right) = 0.21$$

through the electronegativity of atoms in the crystal ($\chi_{\text{Li}} = 0.60$, $\chi_{\text{Al}} = 1.35$, $\chi_{\text{S}} = 2.50$), where $\alpha = 0.18$ [42]. The bonds polarization made

$$P_{\text{LiS}} = 1 - (\chi_{\text{Li}}/\chi_{\text{S}}) = 0.76 \text{ and } P_{\text{AlS}} = 1 - (\chi_{\text{Al}}/\chi_{\text{S}}) = 0.46.$$

Such values of the bonds ionization and polarization indicate that they are both ion-covalent, while the Li-S bond is

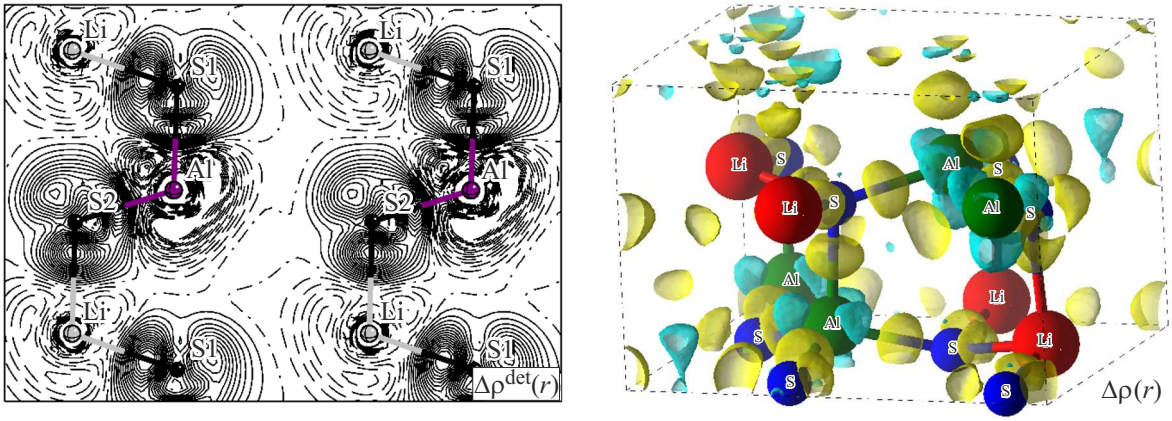

Figure 5. Deformation ($\Delta\rho^{def}(\mathbf{r})$) and difference ($\Delta\rho(\mathbf{r})$) density of distribution of the valence electrons in $LiAlS_2$ crystal.

Table 4. Effective Born charge (in e) in $LiAlS_2$ crystal

Q(Li)	Q(Al)	Q(S1)	Q(S2)
$\begin{pmatrix} 0.98 & 0.12 & 0.02 \\ -0.05 & 1.15 & 0.06 \\ -0.05 & -0.05 & 1.11 \end{pmatrix}$	$\begin{pmatrix} 2.59 & -0.37 & -0.11 \\ 0.25 & 2.51 & -0.34 \\ 0.11 & 0.24 & 2.68 \end{pmatrix}$	$\begin{pmatrix} -1.37 & -0.09 & 0.10 \\ -0.29 & -1.87 & 0.28 \\ 0.13 & 0.38 & -2.22 \end{pmatrix}$	$\begin{pmatrix} -2.20 & 0.34 & -0.08 \\ 0.43 & -1.79 & -0.11 \\ -0.04 & -0.15 & -1.57 \end{pmatrix}$

obviously more ionic. In a 3D distribution model for the valence electrons' charge difference density (Figure 5) the covalent clusters $\Delta\rho(\mathbf{r})$ localized on bonds are also observed, which are more shifted from cations (Li, Al) towards anions (S1 and S2), especially on Li-S bonds.

It can be seen that all of the atoms are surrounded by four atoms of a different kind: Li and Al metals interact with S atoms through the formation of four equivalent donor-acceptor bonds, and the two atoms of Li and two atoms of Al are surrounded by S atoms.

The effective Born charges characterize the polarizability of the bond between atoms when they are shifted from the equilibrium position, and are a dynamic characteristic of the system. Knowing the average value of the diagonal elements of the Born charges the degree of ionic bonding may be estimated. Table 4 shows the effective charge tensors Q(Li), Q(Al), Q(S1) and Q(S2) calculated for $LiAlS_2$. First of all, the summation convention, which is the requirement of charge neutrality, was tested for them:

$$\sum_{k=1}^{N} Q_{k,\alpha\beta} = 0$$

(N — number of atoms in the unit cell). This convention is fulfilled in our calculations: if it's not true this would indicate a convergence problem in the calculations.

The average values of diagonal elements of Born effective charge tensor are $Q_{\mathrm{Li}} = +1.08$; $Q_{\mathrm{Al}} = +2.59$; $Q_{\mathrm{S1}} = -1.82$; $Q_{\mathrm{S2}} = -1.85$, the dynamic charges for unequal sulfur atoms are slightly different because of some difference in the bond lengths of Al-S1, Al-S2 and Li-S1, Li-S2 (Table 2). It is known that for an ideal ionic bond, the dynamic charges of the cation and the anion exactly match their nominal charges, while large difference in their values indicates a strong hybridization of orbitals and availability of the covalent bond. The values of dynamic charges obtained by us are consistent with the nominal charges on the atoms: $+1$, $+3$, and -2, respectively, and in the case of lithium, the values of the average Born and nominal charges are very close. These results also indicate a strong ionic bond between Li-S and Al-S, which is higher on Li-S bond.

The values of diagonal components of the high-frequency permittivity tensor $\varepsilon_\infty(\varepsilon_{xx}, \varepsilon_{yy}, \varepsilon_{zz})$ of the orthorhombic $LiAlS_2$ crystal are equal $\varepsilon_{xx} = 4.375$, $\varepsilon_{yy} = 4.325$, $\varepsilon_{zz} = 4.616$ and comply with the ratios $\varepsilon_{xx} < \varepsilon_{zz}$ and $\varepsilon_{yy} < \varepsilon_{zz}$.

The effective charge tensors Q(Li), Q(Al), Q(S1), and Q(S2) shown in Table 4, were analyzed within the density functional theory using PBE functional and Quantum Espresso program code [31].

6. Lattice dynamics

The energy spectrum of phonons $\omega(\mathbf{k})$ and its spectral density $D(\omega)$ largely determine the structural, thermal, electronic, and optical properties of real substances. Neutron scattering on phonons is considered to be the most informative method of experimental study of collective oscillations. Neutron scattering allows getting the information about the shape of the frequency distribution function and the dispersion law, but this method also has its own theoretical and experimental flaws related to the neutrons-phonons interaction specifics, as well as problems that may arise

Table 5. Frequencies and contributions of sublattices vibrations for $LiAlS_2$, calculated using CRYSTAL (CR) and Quantum Espresso (QE)

Symmetry	$LiAlS_2$					Symmetry	$LiAlS_2$				
C_{2v}^9	QE ω, cm^{-1}	CR ω, cm^{-1}	QE ω, cm^{-1}			C_{2v}^9	QE ω, cm^{-1}	CR ω, cm^{-1}	QE ω, cm^{-1}		
			Li	Al	S				Li	Al	S
	–	–	–	–	–		433	450	13	84	3
	404	422/490	0	31	69		420	427	4	94	2
	394	413/419	1	85	14		375	417	0	31	69
	364	406/410	0	68	32		357	372	48	6	46
	354	361/361	68	1	31		324	354	76	0	24
A_1	316	347/354	86	1	13	A_2	278	330	94	0	6
TO/LO	263	329/340	97	2	1	TO	236	278	9	19	72
	226	263/263	1	1	98		216	214	12	46	42
	195	190/191	6	32	62		159	155	14	4	82
	160	148/148	15	52	33		153	144	8	27	65
	127	113/113	11	6	83		133	123	6	13	81
	115	94/94	12	21	67		109	86	9	22	69
	436	429/509	0	52	48		406	458/496	3	37	60
	400	408/410	2	68	30		397	424/454	2	58	40
	381	405/405	3	75	22		379	411/423	4	94	2
	360	366/369	61	1	38		360	358/371	69	1	30
	323	356/365	77	1	22		337	356/358	75	2	23
B_1	291	346/346	6	2	92	B_2	320	344/345	84	3	13
TO/LO	243	337/339	81	4	15	TO/LO	259	302/303	18	11	71
	199	207/207	5	22	73		200	205/205	13	22	65
	181	196/196	7	14	79		197	171/173	6	33	61
	141	165/165	43	49	8		169	135/135	17	36	47
	96	132/132	14	12	74		134	91/91	8	14	78

during experimental research. In addition, the experimental results largely depend on the quality of the samples and, in particular, on the energy resolution of the spectrometer. Also, one of the problems of the experiment is the difficulty of separating the contributions of coherent and incoherent scattering components. An alternative approach to the study of the crystals phonon spectra is the use of the newly developed theoretical methods based, for example, on the density functional theory (DFT) and the method of molecular dynamics (MD). These methods are implemented in various software codes, including CRYSTAL and Quantum Espresso codes used in this study. This approach makes it possible to study the dynamics of the crystal lattice ab initio, where only minimal input data are needed, including only data on the crystal-forming atoms themselves. Finally, it is possible to obtain and analyze phonon spectra with minimal cost, identify their features due to the chemical composition and structure of the system.

The phonon spectrum $\omega(\mathbf{k})$ at the points of high degree of symmetry of Brillouin zone along X-Γ-Z-U-R-S-Y-T-Z-Γ and the density of states of phonons $D(\omega)$ for $LiAlS_2$ crystal are shown in Figure6. These values were calculated using Quantum Espresso software, in pz approximation.

According to the analysis it was shown that the vibration spectrum of $LiAlS_2$ crystal does not contain any negative frequencies. Consequently, this structure is stable, the crystal has a minimum total energy and can be obtained experimentally, which was confirmed by the successful

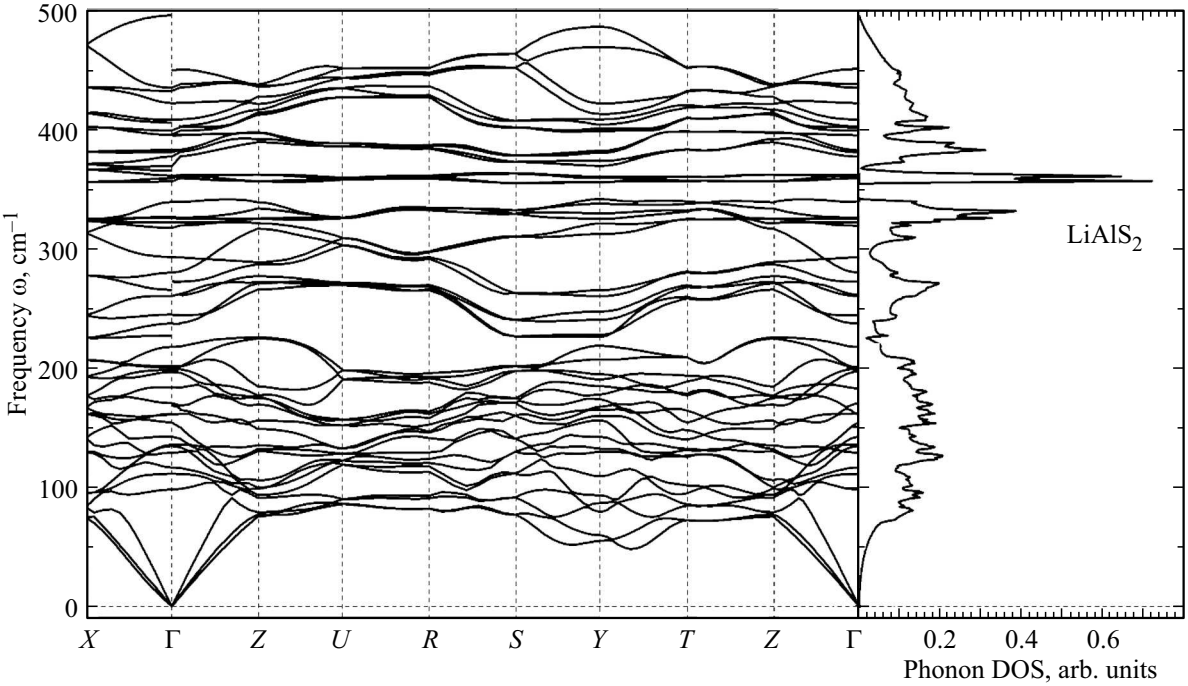

Figure 6. Phonon spectrum $\omega(\mathbf{k})$ (in the left) and density of states of the phonons $D(\omega)$ (in the right) for $LiAlS_2$ crystal.

synthesis as described in [30]. The values of the frequencies of optical phonons in the center of Brillouin zone (point Γ) and the contributions of vibrations of atomic sublattices calculated using CRYSTAL (CR) and Quantum Espresso (QE) codes are given in Table 5.

The vibrational modes found using Quantum Espresso and CRYSTAL codes reflect the qualitative features of collective vibrations in the orthorhombic $LiAlS_2$ crystal and are similar in magnitude. At the same time, the qualitative similarity of the mode distribution in the crystal is preserved. The primitive unit cell of orthorhombic crystals contains sixteen atoms with 48 normal modes in the center of Brillouin zone (Γ point), which can be described as follows:

$$\Gamma_{\text{total}} = 12A_1 + 12A_2 + 12B_1 + 12B_2,$$

where acoustic modes are given by A_1, B_1 and B_2. The remaining 45 optical modes contain 33 vibrational modes active in IR spectrum and 12 active modes in the Raman scattering spectrum (RS, Raman spectrum):

$$\Gamma_{\text{opt}} = 11A_1 + 12A_2 + 11B_1 + 11B_2.$$

The long-range action in crystals due to the Coulomb interaction generates a macroscopic electric field essential for longitudinal (LO) and transverse (TO) optical phonons. The coupling of vibrational modes with an electric field leads to the splitting of longitudinal and transverse modes (LO-TO) in the center of Brillouin zone (Γ point). Group-theoretic analysis and estimate of the percentage contribution of individual atoms to vibrations of a certain symmetry give a complete picture of vibrations in an equilibrium crystal.

The analysis of the atomic sublattice vibrations contribution to the lattice vibrations has shown that optical vibrations with symmetry A_1 and A_2 contain frequencies with almost 100% contribution of atomic vibrations: Li — 263 (329/340−CR) cm^{-1} (97 %) and 278 (330−CR) cm^{-1} (94 %); Al — 420 (427−CR) cm^{-1} (94 %); S — 226 (23/263−CR) cm^{-1} (98 %). Vibrations of Li atoms can be attributed to frequencies with a predominant contribution — 316 (347/354−CR) cm^{-1} (86 %), Al — 394 (413/419−CR) cm^{-1} (85 %), as well as S — 127 (113/113−CR) cm^{-1} (83 %), 133 (123−CR) cm^{-1} (81 %) and 159 (155−CR) cm^{-1} (82 %). Mode A_1 contains a series of vibrations in Al-S bond: 404 (422/490−CR) cm^{-1}, 364 (406/410−CR) cm^{-1}, 195 (190/191−CR) cm^{-1}, 160 (148/148−CR) cm^{-1} and 115 (94/94−CR) cm^{-1}. Li-S bonds correspond to the vibrations with a frequency 354 (361/361−CR) cm^{-1}. For A_2 mode the vibrations in Li-S mode are consistent with the vibrations with frequencies 357 (372−CR) cm^{-1} and 324 (354−CR) cm^{-1}. Also, a series of vibrations inAl-S bond is observed: 375 (417−CR) cm^{-1}, 236 (278−CR) cm^{-1}, 216 (214−CR) cm^{-1}, 153 (144−CR) cm^{-1} and 109 (86−CR) cm^{-1}.

Analyzing the contributions of atomic vibrations in B_1 mode of $LiAlS_2$ crystal, we may see that among 11 frequencies only one may be considered a purely anionic one S — 291 (346/346−CR) cm^{-1} (92 %), another one — contains the predominant contribution of Li atoms vibrations— 243 (337/339−CR) cm^{-1} (81 %). Of the remaining five frequencies the ones that characterize vibrations inAl-S bond: 436 (429/509−CR) cm^{-1},

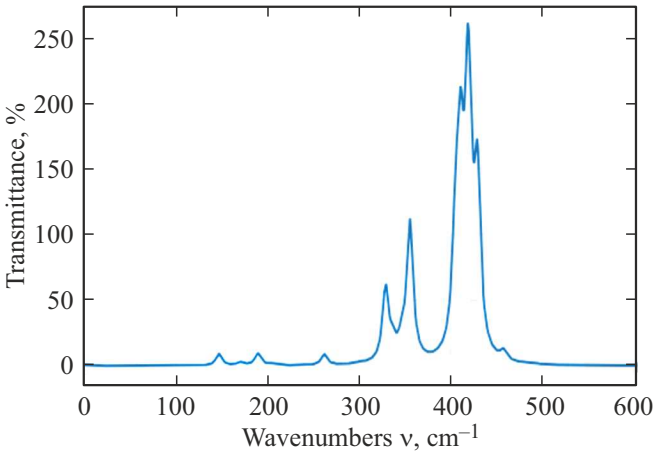

Figure 7. IR-spectrum of $LiAlS_2$.

400 (408/410−CR) cm^{-1}, 381 (405/405−CR) cm^{-1}, 199 (207/207−CR) cm^{-1} and 181 (196/196−CR) cm^{-1}. The rest correspond to the vibrations in Li-S bonds: 360 (366/369−CR) cm^{-1} and 323 (356/365−CR) cm^{-1}. In addition, B_1 mode contains a frequency of 96 (132/132−CR) cm^{-1}, characterizing vibrations of the cation-anion chains Li-S-Al, with a predominant contribution of S atoms(74 %). Frequency 141 (165/165−CR) cm^{-1} also belongs to them and contains almost the same contribution of Li (43 %), Al (49 %) atoms vibrations and a small contribution of S atoms (8 %).

B_2 mode of $LiAlS_2$ crystal mainly characterizes vibrations in the bonds Li-S and Al-S, and contains a single frequency with a high contribution of Al vibrations — 379 (411/423 −CR) cm^{-1} (94 %) and one frequency with a high vibration contribution of Li — 320 (344/345 −CR) cm^{-1} (84 %). B_2 mode also contains the frequency characterizing the vibrations of the cation-anion chains Li-Al-S 169 (135/135−CR) cm^{-1}.

In Raman scattering spectra of $LiAlS_2$ crystal, all modes are active except A_2. The infrared (IR) absorption spectra of the crystal contain the polar modes B_1, B_2 and A_1, split into longitudinal (LO) and transverse (TO) components. The main causes of splitting are the cations-anions interaction and the difference in atomic masses (a.e.m.): 7 (Li), 27 (Al) and 32 (S), which is manifested in the vibration amplitudes of individual atoms in the corresponding sublattices, as well as in the vibrations of cation-anion pairs (Li-S and Al-S), which determine the bonds in the cationic tetrahedra of LiS_4 and AlS_4.

In [30], it is reported that IR spectrum of the orthorhombic crystal $LiAlS_2$ was measured, but the authors do not provide any experimental data. Greater attention is paid to measuring LIDT (laser-induced damage threshold) in $LiAlS_2$ crystal under the influence of pulsed laser radiation (2.09 μm, 50 nc, 3 Hz) performed using the single pulse method. As a result of the experiment, it was found that, compared with the reference $AgGaS_2$ crystal, under the same conditions, the sample of $LiAlS_2$ demonstrates an ultra-high LIDT destruction threshold (approximately 28, times higher than $AgGaS_2$).

Table 6. Distribution of phase velocities (in m/s) over the wave vectors

	[001]	[010]	[100]	[110]	[101]	[011]	[111]
υ_P	6081	5616	5983	6157	5716	5978	5971
υ_{S1}	3304	3395	3395	3074	3418	3122	3424
υ_{S2}	2824	3304	2824	2699	3350	3072	2769

Using IR-spectrum simulator [43], and based on the data obtained using CRYSTAL code, we've obtained the IR-spectrum of $LiAlS_2$ crystal within the frequency range from 0 to 600 cm^{-1} with its graph shown in Figure 7.

As seen from the figure, the IR-spectrum of $LiAlS_2$ crystal contains three major groups: the first one — within the range 130−260 cm^{-1}, which generally, contains vibrations of sublattices of individual atoms S, Al and Li and cation-anion chains like -Li-Al-S-; the second one — within the range 330−380 cm^{-1} contains the predominant vibrations of the cation-anion pairsAl-S and Li-S; the third one — within the range 400−480 cm^{-1} generally corresponds to the vibrations of light metals Li and Al, as well as Al-S bonds. In general, the obtained results are consistent with the data of RS spectra for the equivalent orthorombic crystals of LiMS$_2$ (M = Al, Ga, In) family [44], in particular, in terms of the frequency bands and the availability of oscillatory modes in them. First group — near 100 cm^{-1}; second group — within 250−350 cm^{-1} for sulfides; third group — within 350−450 cm^{-1} (sulfides) [44].

The phase velocities found for the major directions using CRYSTAL program code are given in Table 6. Sound wave velocities are associated, for instance, with such a physical property as thermal conductivity, which defines the area of practical application of $LiAlS_2$ crystal. Elastic waves propagating in the crystals are classified as three phase velocities, where two of them — being quasi-transverse (υ_{S1}, υ_{S2}) and another one — quasi-longitudinal (υ_P).

7. Mechanical properties

Mechanical properties of tetragonal Li-contaning crystals with a halcopiryte structure $LiGaSe_2$ [45] and LiMS$_2$ (M = B, Al, Ga, In, Tl) [35], which are equivalents of the orthorhombic $LiAlS_2$ structure were studied based on ab initio analysis and allowed estimating the stability and strength of the tetragonal crystals. In this study using CRYSTAL code and the same method we've calculated the elastic constants (C_{ij}), basic elasticity modulus (E, G, K), Poisson ratio (ν) of the orthorhombic $LiAlS_2$ crystal, and also additionally found Cauchy pressures (p_a, p_b, p_c) (in GPa), microhardness (H) and Gruneisen parameter (γ_G) (in GPa), shift anisotropy coefficients (A_1, A_2, A_3)

Table 7. Parameters characterizing mechanical properties of $LiAlS_2$ crystal (in GPa)

C_{11}	C_{12}	C_{13}	C_{22}	C_{23}	C_{33}	C_{44}	C_{55}	C_{66}	ν
70.02	37.21	25.38	61.70	29.71	72.33	21.36	15.60	22.55	0.309

E	G	K	K/G	G/K	H_m	H_v	γ_G	A_1	A_2	A_3	A_U
49.47	18.89	43.20	2.29	0.44	2.41	2.88	1.83	0.93	0.84	1.57	0.24

and universal anisotropy factor (A^U). The obtained values are listed in Table 7. Also the fundamental physical characteristics of the studied orthorhombic $LiAlS_2$ crystal were first introduced: Yung modulus E, shear modulus G, uniform compression modulus K and Poisson ratio ν.

Based on the obtained data we may conclude that $LiAlS_2$ crystal in its orthorhombic phase is steady which is proved by the calculated elastic constants meeting the Born conditions [46–48] for the orthorhombic crystals. All diagonal components of elastic constants are positive [46]

$$C_{ii} > 0 \ (i = 1, 4, 5, 6),$$

and the ratios are also fulfilled.

$$C_{11}C_{22} > C_{12}^2, \quad C_{22}C_{33} > C_{23}^2, \quad C_{11}C_{33} > C_{13}^2,$$

$$C_{11}C_{22}C_{33} + 2C_{12}C_{13}C_{23} - C_{11}C_{23}^2 - C_{22}C_{13}^2 - C_{33}C_{12}^2 > 0.$$

Since the fulfillment of the Born criteria guarantees basic mechanical stability only formally, in relation to infinitely small deformations, then, along with the fulfillment of the Born criteria, it is necessary to calculate the Cauchy pressures, which for orthorhombic phases are found by the formulas [49]:

$$p_a = C_{23} - C_{44}, \quad p_b = C_{12} - C_{66}, \quad p_c = C_{13} - C_{55}.$$

Depending on the sign of the calculated pressures, two cases of manifestation of such mechanical properties as brittleness and plasticity are possible: if $p > 0$, then the body exhibits plastic properties; if $p < 0$, then the material is prone to brittle fracture. Since the studied compound has positive Cauchy pressure values ($p_a = 8.35$, $p_b = 14.67$, $p_c = 9.78$), therefore, the orthorhombic $LiAlS_2$ crystal is featuring plasticity properties.

The Poisson's ratio ν and the Pugh criterion [50], in addition to the conditions considered, supplement the information on the brittleness and plasticity of $LiAlS_2$ crystal, for which the relations $K/G \geq 1.75$ and, respectively, $G/K \leq 0.57$ [51], which also means that $LiAlS_2$ is itself a durable and ductile material.

The coefficients of shear anisotropy make it possible to measure the degree of anisotropy in the bonds between atoms in various planes [52]. The coefficient of shear anisotropy for the shear planes (100) between directions (011) and (010) is equal to:

$$A_1 = 4C_{44}/(C_{11} + C_{33} - 2C_{13}),$$

for the shear planes (010) between the directions (101) and (001) it is equal:

$$A_2 = 4C_{55}/(C_{22} + C_{33} - 2C_{23}),$$

and for the shear planes (001) between the directions (110) and (010) it is equal:

$$A_3 = 4C_{66}/(C_{11} + C_{22} - 2C_{12}).$$

The coefficients of shear anisotropy obtained in our study are also shown in Table 7. For an isotropic crystal, the coefficients A_1, A_2 and A_3 must be equal to unity, while any value less than or greater than unity is a measure of the degree of elastic anisotropy that the crystal possesses. If the studied crystal may be dubbed an almost isotropic crystal in the directions (100) and (010), then in the direction (001) it has a large shear anisotropy.

On the other hand, the universal Zener anisotropy index [53]:

$$A^U = 5G_V/G_R + K_V/K_R - 6,$$

where G_V, G_R, K_V, K_R — the shear modulus and the Voigt and Reuss uniform compression modulus also indicate a slight anisotropy. This is because A^U is identically zero for the locally isotropic single crystals, and its deviation from zero determines the degree of anisotropy of a single crystal and takes into account both the contribution of shear and volumetric deformations, unlike all existing measures of anisotropy.

The graphical image of anisotropy of the modeled crystal elastic properties was obtained using open ELATE software: Elastic tensor analysis [54]. For this purpose, closed three-dimensional (3D) isosurfaces of the Young's modulus (E) and compressibility ($\beta = 1/K$) were constructed (Figure 8), in the coordinate space x, y and z, showing the deviation of these surfaces from the spherical shapes typical of isotropic materials.

The strength and stability of a material are directly related to its resistance to the outer mechanical loads described as a microhardness which is basically found from the experiment, generally by indenting the diamond pyramids or steel balls into a real-life specimen. The microhardness was found by the formula [55]:

$$H_m = E(1 - 2\nu)/6(1 + \nu).$$

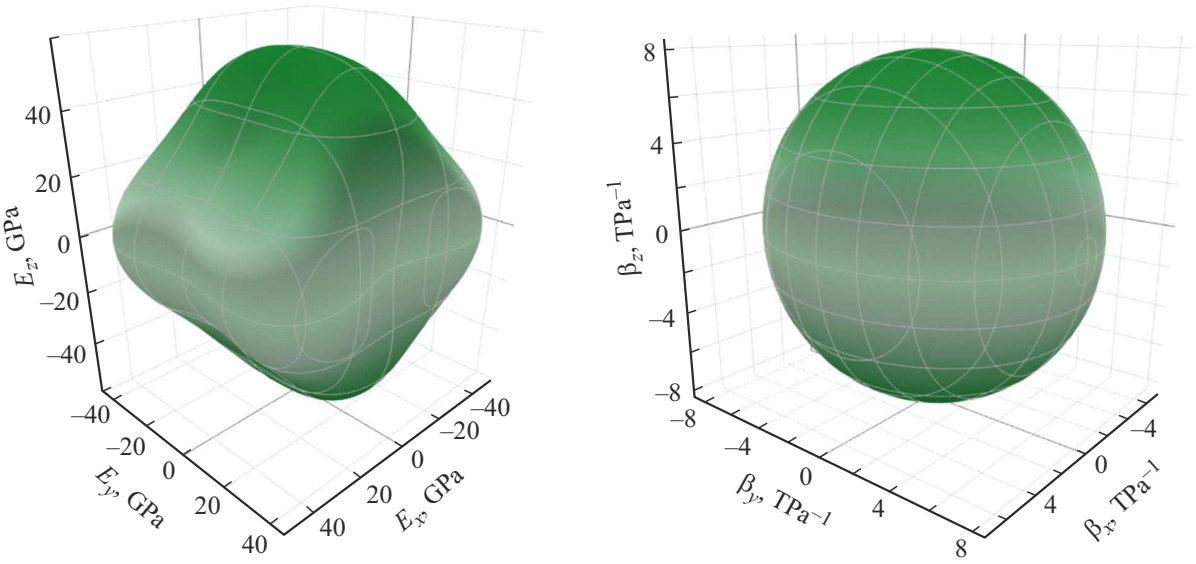

Figure 8. 3D-surface of Young's modulus E — in the left and compressibility modulus β — in the right for $LiAlS_2$ crystal.

Vickers microhardness H_v characterizes the ability of a material to resist deformation under compressive stresses and can be calculated using the empirical formula [56]:

$$H_v = 0.92(G/K)^{1.137}G^{0.708}.$$

The difference between the theoretical values of H_v and H_m is due to the choice of the calculation method and the parameters involved in the computational formulas. Judging by microhardness, the crystal belongs to fairly durable and stable materials. This finding is also supported by conclusions based on the ratios of shear modulus and uniform compression ($K/G \geq 1.75$ and $G/K \leq 0.57$).

A measure of thermodynamic stability of a crystal can be a change in the lattice enthalpy, since this change determines the amount of energy needed to break chemical bonds between atoms and, therefore, determines the energy of formation of the crystal lattice. The larger the enthalpy the stronger the chemical bond and the more stable the crystal state.

Within DFT theory using the self-consistency analysis in QE software and applying PBE functional the bond energy was calculated for the studied compounds with a chalcopyrite structure [57] ΔH:

$$\Delta H = (E_{\text{full}} - \Sigma n_i \cdot E_i)/m,$$

where E_{full} — energy of the system with chalcopyrite structure; n_i and E_i — quantity and energy of i-th component in the system; m — general amount of atoms in the system. All energies are calculated for their stable solid phase. Negative (positive) enthalpy of formation indicates the stability (instability) of the system. The bond energy found using method from [57] provided the following value of $LiAlS_2$ (-3.42 eV/f.u.). When estimating the enthalpy variations [58] it was found that enthalpy was negative 337 kJ/mol at 300 K.

Found by the formula from [59]

$$\gamma_G = 3(1+\nu)/2(2-3\nu)$$

the Gruneisen parameter of the studied crystal lies within the commonly known range 0.85−3.53 of the interatomic interaction anharmonicity.

8. Conclusion

Modelling using two fundamentally different approaches in CRYSTAL and Quantum Espresso, based on the functional density theory, allowed to get a potential variety of data on the spread of values of the lattice parameters a, b, c of the orthorhombic $LiAlS_2$ crystal, which in both cases are comparable with the experimental data. The coordinates of non-equivalent atoms are first introduced and the bond lengths Li-S and Al-S are specified. Based on this equilibrium parameters of the lattice all further calculations were made. The calculated energy band structure of the orthorhombic $LiAlS_2$ crystal and its sub-lattices, using different functionals and approximations for CRYSTAL and Quantum Espresso demonstrated a common similarity in the valence bands, its vertices and conduction band bottom. It was illustrated that the crystal band structure is formed largely depending on the sub-lattice states. A more precise and close to the experiment result gives the bang gap width E_g (4.58 eV) in CRYSTAL in combination of PBE functional with the full-electron valence-split basis of Gaussian orbitals TZVP. The performed studies of vibrational and elastic properties of $LiAlS_2$ crystal showed the absence of negative vibrational modes, and for the elastic constants — full compliance with Born conditions was demonstrated. The dependability and stability of $LiAlS_2$ orthorhombic crystal was proved by complying with all necessary elasticity theory

conditions, positive values of optical vibrations within the frequencies spectra and negative enthalpy of the crystal formation process. The findings demonstrated the need and reliability of the ab initio analysis.

Conflict of interest

The authors declare no conflict of interest.

References

[1] E.E. Hellstrom, R.A. Huggins. Mat. Res. Bull. **14**, 881 (1979).
[2] L. Isaenko, A. Yelisseyev, S. Lobanov, V. Petrov, F. Rotermund, J.-J. Zondy, G.H.M. Knippels. Mater. Sci. Semicond. Processing **665**, 4 (2001).
[3] L. Isaenko, A. Yelisseyev, S. Lobanov, V. Petrov, F. Rotermund, G. Slekys, J.-J. Zondy. J. Appl. Phys. **91**, 9475 (2002).
[4] L. Isaenko, A. Yelisseyev, S. Lobanov, A. Titov, V. Petrov, J.-J. Zondy, P. Krinitsin, A. Merkulov, V. Vedenyapin, J. Smirnova. Cryst. Res. Technol. **38**, *3–5*, 379 (2003).
[5] A. Yelisseyev, F. Liang, L. Isaenko, S. Lobanov, A. Goloshumova, Z.S. Lin. Optical Materials **72**, 795e804 (2017).
[6] L. Kang, M. Zhou, J. Yao, Z. Lin, Yi. Wu, C. Chen. J. Am. Chem. Soc., **137**, 13049 (2015).
[7] A. Abudurusuli, J. Huang, P. Wang, Z. Yang, S. Pan, J. Li Angew. Chem. Intl. Edit., **60**, 24131 (2021).
[8] H. Zhang, M. Zhang, S. Pan, X. Dong, Z. Yang, X. Hou, Z. Wang, K.B. Chang, K.R. Poeppelmeier. J. Am. Chem. Soc. **137**, 8360 (2015).
[9] K. Wu, Y. Yang, L. Gao. Coord. Chem. Rev. **418**, 213380 (2020).
[10] G. Li, Z. Yang, J. Li, J. Li, S. Pan. Chem. Commun. **56**, 11565 (2020).
[11] W. Xing, N. Wang, C. Tang, C. Li, Z. Lin, J. Yao, W. Yin, B. Kang. J. Mater. Chem. C **9**, 1062 (2021).
[12] F. Chiker, B. Abbar, A. Tadjer, H. Aourag, B. Khelifa. Mater. Sci. Eng. B **98**, 81 (2003).
[13] L. Bai, Z.S. Lin, Z.Z. Wang, C.T. Chen. J. Appl. Phys. **103**, 083111 (2008).
[14] S. Wang, H. Ruan, G. Liu, G. Zhang, Q. Shi, X. Zhang, Z. Gao, C. Dong, X. Tao. J. Cryst. Growth **362**, 271 (2013).
[15] G.M. Dongho-Nguimdo, E. Igumbor, S. Zambou, D.P. Joubert. Comput. Condens. Matter **21**, e00391 (2019).
[16] A. Khan, M. Sajjad, G. Murtaza, A. Laref, Z. Naturforsch. A **73**, 645 (2018).
[17] E.B. Duginova, Yu.M. Basalayev. Electronnoye stroyeniye ortorombicheskikh kristallov $LiMTe_2$ (M = Al, Ga, In; X = O, S, Se). Red.mag.„Izv. vuzov. Fysika“, Tomsk, (2009) 41 p. Dep. in VINITI, 20.04.2009, № 230-B2009. (in Russian).
[18] E.B. Duginova. Energeticheskaya structura i khimicheskaya svyaz v metallakh $LiMX_2$ (M = Al, Ga, In; X = S, Se, Te) i $LiGaO_2$: Dis. kand. fiz.-mat. nauk. Kemerovo, (2009). 124 p. (in Russian).
[19] F. Liang, L. Kang, Z. Lin, Y. Wu, C. Chen. Coord. Chem. Rev. **333**, 57 (2017).
[20] Z. Wang, Y. Pan, T. Li, K. Wu, T. Rao, L. Hu, Y. Feng, C. Yang. Physica B. **626**, 413531 (2022).
[21] S. Liu, W. Chen, C. Liu, B. Wang, H. Yin. Results Phys. **26**, 104398 (2021).
[22] Y. Fan, X. Song, S. Qi, X. Ma, M. Zhao. J. Mater. Chem. A. **7**, 26123 (2019).
[23] W. Xu, R. Wang, B. Zheng, X. Wu, H. Xu. J. Phys. Chem. Lett. **10**, 6061 (2019).
[24] Q. Lv, J. Qiu, Q. Wen, D. Li, Y. Zhou, G. Lu. Mater. Sci. Semicond. Process. **154**, 107222 (2023).
[25] K.Q. Abbasi, R.W.A. Havenith, Z. Rashid. ACS Appl. Energy Mater. **7**, 7432 (2024).
[26] R. Maphanga, M.S. Santosh, E. Rugut, S. Dima, P. Mondal, P. Maleka, D. Tshwane, E. Maluta, S. Rtimi. Comput. Mater. Sci. **248**, 113576 (2025).
[27] L. Isaenko, I. Vasilyeva, A. Merkulov, A. Yelisseyev, S. Lobanov. J. Cryst. Growth **275**, 217 (2005).
[28] H. Lim, S.-C. Kim, J. Kim, Y.-I. Kim, S.-J. Kim. J. Sol. S. Chem. **257**, 19 (2018).
[29] M.L.H. Chandrappa, J. Qi, C. Chen, S. Banerjee, S.P. Ong. J. Am. Chem. Soc. **144**, 18009 (2022).
[30] G. Li, Z. Yang, S. Pan. Sci. China Mater., **66**, *3*, 1189 (2023).
[31] S. Baroni, S. de Gironcoli, A. Dal Corso, P. Giannozzi. Rev. Mod. Phys. **73**, 515 (2001).
[32] R. Dovesi, R. Orlando, B. Civalleri, C. Roetti, V.R. Saunders, C.M. Zicovich-Wilson, **220**, 571 (2005).
[33] W. Setyawan, S. Curtarolo. Computational Materials Science. **49**, 299 (2010).
[34] K. Momma, F. Izumi. J. Appl. Crystallogr. **44**, 1272 (2011).
[35] Y.M. Basalaev, E.B. Duginova, S.A. Marinova. Solid State Commun. **409**, 116264 (2026).
[36] Y.N. Zhuravlev, A.S. Poplavnoy. ZhSKh **42**, *5*, 860 (2001).
[37] Yu.M. Basalaev, Yu.N. Zhuravlev, A.V. Kosobutsky, A.S. Poplavnoy. FTT **46**, *5*, 826 (2004) (in Russian).
[38] A.S. Poplavnoy, A.V. Silinin. Krystallografia **50**, *5*, 782 (2005) (in Russian).
[39] Y.N. Zhuravlev Issledovaniye electronnoy struktury i khimicheskoy svyazi ryadov preimuchsestvenno ionnykh i ionno-molekulyarnykh krystallov po metodu podreshetok: Dis. dokt. fiz.-mat. nauk. Kemerovo, (2003). p. 357 (in Russian).
[40] Yu.M. Basalaev, A.S. Poplavnoy. ZhSKh **50**, *6*, 1232 (2009).
[41] Y.N. Zhuravlev, A.S. Poplavnoy. FTT **43**, *11*, 1984 (2001) (in Russian).
[42] S.S. Batsanov. Strukturnaya khimiya (facty i zavisimosti). M. Dialog-MGU (2000). p. 291 (in Russian).
[43] https://crysplot.crystalsolutions.eu, 2025.
[44] L.I. Isaenko, A.P. Yelisseyev. Semicond. Sci. Technol. **31**, 123001 (2016).
[45] Y.M. Basalaev, E.B. Duginova, E.V. Duginov, O.G. Basalaeva. Solid State Commun. **403**, 116005 (2025).
[46] H. Neumann. Cryst. Res. Technol. **39**, *11*, 939 (2004).
[47] A.I. Gusev, S.I. Sadovnikov. FTT **6**, 671 (2022) (in Russian).
[48] F. Mouhat, F.-X. Coudert. Phys. Rev. B **90**, 224104 (2014).
[49] Y. Wu, Y. Duan, X. Wang, M. Peng, Li Shen, H. Qi. Mater. Today Commun. **33**, 104651 (2022).
[50] S.F. Pugh. Lond. Edinb. Dubl. Phil. Mag. & J. Sci. **45**, *367*, 823 (1954).
[51] I.Yu. Grubova, R.A. Surmenev, E.C. Neyts, A.V. Koptyug, A.P. Volkova, M.A. Surmeneva. ACS Omega **8**, 27519 (2023).
[52] P. Ravindran, Lars Fast, P.A. Korzhavyi, B. Johansson, J. Wills, O. Eriksson. J. Appl. Phys. **84**, *9*, 4891 (1998).
[53] S.I. Ranganathan, M. Ostoja-Starzewski. Phys. Rev. Lett. **101**, 055504 (2008).

[54] R. Gaillac, P. Pullumbi, F.-X. Coudert. J. Phys. Condens. Matter, **28**, 275201 (2016).
[55] El-S. Yousef, A. El-Adawy, N. El-K. Khany. Solid State Commun. **139**, 108 (2006).
[56] Y. Tian, B. Xu, Z. Zhao. J. Refract. Met. Hard Mater. **33**, 93 (2012).
[57] N. Kim, P.P. Martin, A.A. Rockett, E. Ertekin. Phys. Rev. B. **93**, 165202 (2016).
[58] A.S. Verma. Philos. Mag. **89**, 183 (2009).
[59] V.N. Belomestnykh, E.P. Tesleva. J. Tech. Phys. **49**, 1098 (2004).

Translated by T.Zorina